

Journal of
Mechanics of
Materials and Structures

**WAVELET SPECTRAL ELEMENT FOR WAVE PROPAGATION
STUDIES IN PRESSURE LOADED AXISYMMETRIC CYLINDERS**

Mira Mitra and S. Gopalakrishnan

Volume 2, N° 4

April 2007



mathematical sciences publishers

WAVELET SPECTRAL ELEMENT FOR WAVE PROPAGATION STUDIES IN PRESSURE LOADED AXISYMMETRIC CYLINDERS

MIRA MITRA AND S. GOPALAKRISHNAN

We study transient wave propagation in a pressure loaded isotropic cylinder under axisymmetric conditions. A 2-D wavelet based spectral finite element (WSFE) is developed to model the cylinder with radial and axial displacements. The method involves a Daubechies compactly supported scaling function approximation in the temporal dimension and one spatial (axial direction) dimension. This reduces the governing partial differential wave equation into a set of variable coefficient ODEs, which are then solved using Bessel's function approximation. This spectral method captures the exact inertial distribution and thus results in large computational savings compared to the conventional finite element (FE) formulation. In addition, the use of localized basis functions in the present formulation circumvents several serious limitations of the previous FFT based techniques. Here, the proposed method is used to study radial and axial wave propagation in cylinders with different configurations. The analysis is performed in both time and frequency domains. The time domain responses are validated with 2-D FE results.

1. Introduction

Wave propagation analysis in cylindrical structures is of much relevance for its applications to problems like health monitoring of fluid carrying pipes, excavation casings, and so on [Yin and Yue 2002; El-Raheb 2005]. Recently, with the advent of carbon nanotubes, researchers have been working towards dynamic and wave propagation analyses [Mahan 2002; Wang et al. 2005] of hollow cylindrical shells resembling the carbon nanotube configuration.

Wave propagation problems deal with high frequency excitations and the FE modeling is not computationally viable here as the element size has to be comparable to wavelengths, which are very small at higher frequencies. This results in large system size, and thus alternative numerical schemes [Bao et al. 1999; Godinho et al. 2003; 2004] are generally developed, which are highly accurate in numerical differentiation and also computationally efficient. The FFT based Spectral Finite Element (FSFE) [Doyle 1999] is one such technique specially formulated for wave propagation analysis, and it follows the FE procedure in the transformed frequency domain. In FSFE for 2-D problems, the nodal displacements are related to the nodal forces through a frequency-wavenumber dependent dynamic stiffness matrix. It captures the mass distribution accurately and hence makes it possible to derive the exact elemental matrix. Thus in the absence of discontinuities, a single element is sufficient to model the 2-D structure of any length but unbounded along one spatial dimension.

The main drawback of FSFE is that it cannot handle waveguides of short lengths. This is because the periodicity assumption in the time approximation results in wrap-around for smaller time windows, which totally distorts the response. In addition, for 2-D problems, FSFE are essentially semi-infinite, that

Keywords: wave propagation, wavelets, spectral finite element, axisymmetry.

is, bounded in only one direction. Thus the effect of one spatial boundary cannot be captured and this is attributed to the global nature of the basis functions of the Fourier series approximation of the spatial dimension. However, in Wavelet based Spectral Finite Element (WSFE) [Mitra and Gopalakrishnan 2005], use of localized Daubechies [1992] compactly supported wavelets as basis functions removes the wrap-around problem and can efficiently model undamped structures of finite length. For 2-D problems WSFE [Mitra and Gopalakrishnan 2006c; 2006b] can accurately model structures of finite dimensions. This is again due to the use of localized Daubechies scaling functions as the basis for approximation of spatial dimension.

The governing differential equations for axisymmetric structures have variable coefficients. Thus the 2-D WSFE formulation for these problems is different from that for WSFE for plates [Mitra and Gopalakrishnan 2006c; 2006b]. Here, unlike plates, the reduced ODEs obtained after transformations of the PDEs are variable coefficient equations which have Bessel's function as their solution. Hence, the shape functions are obtained in terms of Bessel's functions. The formulation of the elemental dynamic stiffness matrix from these shape functions is very similar to that in FE.

As in the case of 2-D FSFE, the frequency dependent wave characteristics corresponding to each spatial (axial) wavenumber, can be extracted from our WSFE formulation. However, unlike FSFE, the wavenumbers will be accurate only up to a certain fraction of the Nyquist frequency [Mitra and Gopalakrishnan 2006a]. In addition, here the governing PDE involves variable coefficients as a function of the radius and hence the spectrum relations are derived for a certain radius following a similar procedure as for the WSFE method for plates. Thus the frequency dependent spectrum relation obtained for such axisymmetric problems varies for both axial wavenumbers and the radius.

The paper is organized as follows. Section 2 elaborates the reduction of PDEs to ODEs, Section 3 contains the frequency domain analysis and Section 4 the spectral finite element formulation. Numerical results for time and frequency domains for different cylinder configurations are presented in Section 5. The simulated responses are validated with 2-D FE analysis. The paper ends with important conclusions.

2. Reductions of wave equations to ODEs

The steps followed in 2-D WSFE for an axisymmetric cylinder are as follows. Here, first the Daubechies scaling functions are used for approximation in time and this reduces the governing PDEs with variable coefficients into a set of coupled PDEs in spatial dimensions. The wavelet extrapolation technique proposed by Williams and Amaratunga [1997] is used for adapting wavelets in the finite domain and the imposition of initial conditions. The coupled transformed PDEs are decoupled through eigenvalue analysis. Though the eigen analysis involved is time consuming, this can be computed and stored as it is not dependent on the particular problem. Next, each of these decoupled PDEs are further reduced to a set of coupled ODEs by using the same Daubechies scaling functions for approximation in the spatial dimension. Unlike the temporal approximation, here, the scaling function coefficients lying outside the finite domain are not extrapolated but obtained through periodic extension for unrestrained (free) axial edges. In this paper, the formulation and examples are presented only for unrestrained axial boundary conditions. However, other boundary conditions such as fixed-fixed or free-fixed can also be imposed through a restrain matrix [Mitra and Gopalakrishnan 2006c]. Each set of these ODEs is coupled, and here decoupling can only be done for unrestrained boundary conditions. As said earlier, these decoupled ODEs have coefficients

that vary with the radius. Here, the Bessel function solution is used as interpolating functions and the elemental dynamic stiffness matrix is obtained using these functions. The above mentioned steps are discussed in detail in the following subsections.

2.1. Governing differential equations. The governing differential equations for a hollow cylindrical structure are generally written in cylindrical coordinate system (r, θ, z) , which denotes the radial, circumferential and axial directions. The displacement components are u, v and w in the radial, circumferential and axial directions. For the axisymmetric condition, the circumferential displacement v and the variations of the other two displacements with respect to θ are not considered in the modeling. Thus the equations of motion for an axisymmetric isotropic hollow cylinder contain only displacements u, w with variations along r, z (see Figure 1) and time t , and can be written as

$$\begin{aligned}
 (\lambda + 2\mu)\nabla_0^2\Delta &= \rho \frac{\partial^2\Delta}{\partial t^2}, \\
 c_d^2\nabla_0^2\Delta &= \frac{\partial^2\Delta}{\partial t^2}, \quad c_d^2 = (\lambda + 2\mu)/\rho,
 \end{aligned}
 \tag{1}$$

$$\begin{aligned}
 \mu\nabla_1^2\mathcal{U}_\theta &= \rho \frac{\partial^2\mathcal{U}_\theta}{\partial t^2}, \\
 c_s^2\nabla_1^2\mathcal{U}_\theta &= \frac{\partial^2\mathcal{U}_\theta}{\partial t^2}, \quad c_s^2 = \mu/\rho,
 \end{aligned}
 \tag{2}$$

where ∇_n^2 , for subscripts $n = 0$ and 1 , is defined by

$$\nabla_n^2 \equiv \frac{\partial^2}{\partial r^2} + \frac{1}{r} \frac{\partial}{\partial r} - \frac{n^2}{r^2} + \frac{\partial^2}{\partial z^2}.$$

The variables Δ and \mathcal{U}_θ are dilation and rotation vectors reduced for axisymmetric motions as

$$\Delta = \frac{1}{r} \frac{\partial(ru)}{\partial r} + \frac{\partial w}{\partial z}, \quad \mathcal{U}_\theta = \frac{\partial u}{\partial z} - \frac{\partial w}{\partial r},
 \tag{3}$$

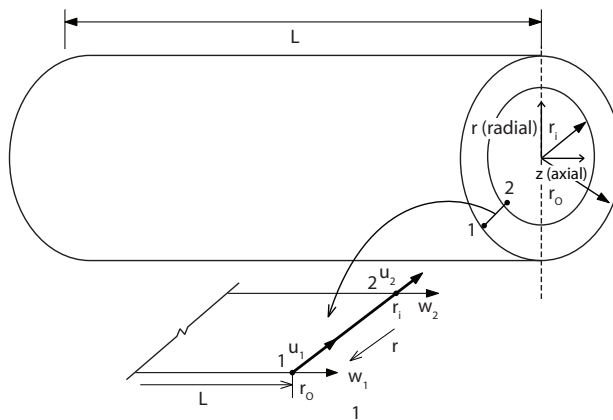


Figure 1. Axisymmetric element with nodal displacements and forces.

and λ, μ are the Lamé’s constants and ρ is the mass density. From Equations (3), the displacements can be written in decoupled form as

$$\nabla_1^2 u = \frac{\partial \Delta}{\partial r} + \frac{\partial \bar{U}_\theta}{\partial z}, \quad \nabla_0^2 w = \frac{\partial \Delta}{\partial z} - \frac{1}{r} \frac{\partial (r \bar{U}_\theta)}{\partial r}. \tag{4}$$

The associated boundary conditions are

$$\sigma_r = \lambda \Delta + 2\mu \frac{\partial u}{\partial r}, \quad \sigma_z = \mu \frac{\partial u}{\partial z} + \frac{\partial w}{\partial r}, \tag{5}$$

where σ_r and σ_z are the radial and axial forces acting on the surface of the cylinder along the z direction.

2.2. Daubechies compactly supported wavelets. A concise review of orthogonal basis of Daubechies wavelets Daubechies 1992 is provided. The wavelets $\psi_{j,k}(t)$ form compactly supported orthonormal basis for $L^2(\mathbb{R})$. The wavelets and the associated scaling functions $\varphi_{j,k}(t)$ are obtained by translation and dilation of single functions $\psi(t)$ and $\varphi(t)$:

$$\psi_{j,k}(t) = 2^{j/2} \psi(2^j t - k), \quad \varphi_{j,k}(t) = 2^{j/2} \varphi(2^j t - k), \quad j, k \in \mathbb{Z}.$$

The scaling functions $\varphi(t)$ are derived from the dilation or scaling equation,

$$\varphi(t) = \sum_k a_k \varphi(2t - k),$$

and the wavelet function $\psi(t)$ is obtained as

$$\psi(t) = \sum_k (-1)^k a_{1-k} \varphi(2t - k).$$

The a_k are the filter coefficients and are fixed for specific wavelet or scaling function basis. For compactly supported wavelets only a finite number of a_k are nonzero. The filter coefficients a_k are derived by imposing certain constraints on the scaling functions which are as follows. (1) The area under scaling function is normalized to one. (2) The scaling function $\varphi(t)$ and its translates are orthonormal. (3) The wavelet function $\psi(t)$ has M vanishing moments. The number of vanishing moments M denotes the order N of the Daubechies wavelet, where $N = 2M$.

Let $P_j(f)(t)$ be the approximation of a function $f(t)$ in $L^2(\mathbb{R})$ using $\varphi_{j,k}(t)$ as a basis, at a certain level (resolution) j . Then

$$P_j(f)(t) = \sum_k c_{j,k} \varphi_{j,k}(t), \quad k \in \mathbb{Z},$$

where the $c_{j,k}$ are the approximation coefficients.

2.3. Temporal approximation. The first step of formulation of WSFE is the reduction of each of the two governing differential equations (1) and (2) with variables Δ and \bar{U}_θ , to a set of PDEs in spatial dimensions by Daubechies scaling function based transformation in time. The procedure has been discussed earlier in [Mitra and Gopalakrishnan 2005; 2006c] for WSFE formulation for beams and plates, respectively and is described here in brief for completeness. Let $\Delta(r, z, t)$ be discretized at n points in the time window $[0, t_f]$. Let $\tau = 0, 1, \dots, n - 1$ be the sampling points; then

$$t = \Delta t \tau,$$

where Δt is the time interval between two sampling points. The function $\Delta(r, z, t)$ can be approximated by the scaling function $\varphi(\tau)$ at an arbitrary scale as

$$\Delta(r, z, t) = \Delta(r, z, \tau) = \sum_k \Delta_k(r, z) \varphi(\tau - k), \quad k \in \mathbb{Z},$$

where the $\Delta_k(r, z)$ (written Δ_k hereafter) are the approximation coefficients at spatial coordinates r and z and (1) can be written as

$$\sum_k c_d^2 \left(\frac{\partial^2}{\partial r^2} + \frac{1}{r} \frac{\partial}{\partial r} + \frac{\partial^2}{\partial z^2} \right) \Delta_k \varphi(\tau - k) = \frac{1}{\Delta t^2} \sum_k \Delta_k \varphi''(\tau - k). \tag{6}$$

Taking the inner product of both sides with the translates of scaling functions $\varphi(\tau - j)$, where $j = 0, 1, \dots, n - 1$ and using their orthogonal properties, we get n simultaneous PDEs:

$$c_d^2 \left(\frac{\partial^2}{\partial r^2} + \frac{1}{r} \frac{\partial}{\partial r} + \frac{\partial^2}{\partial z^2} \right) \Delta_j = \frac{1}{\Delta t^2} \sum_{k=j-N+2}^{j+N-2} \Omega_{j-k}^2 \Delta_k, \quad j = 0, 1, \dots, n-1, \tag{7}$$

where N is the order of the Daubechies wavelet and the Ω_{j-k}^2 are the connection coefficients, defined by

$$\Omega_{j-k}^2 = \int \varphi''(\tau - k) \varphi(\tau - j) d\tau. \tag{8}$$

Similarly, for the first-order derivative, the Ω_{j-k}^1 are defined by

$$\Omega_{j-k}^1 = \int \varphi'(\tau - k) \varphi(\tau - j) d\tau.$$

For compactly supported wavelets, $\Omega_{j-k}^1, \Omega_{j-k}^2$ are nonzero only in the interval $k = j - N + 2$ to $k = j + N - 2$. The detail for evaluation of connection coefficients for different derivative orders is given in [Beylkin 1992].

It can be observed from the PDEs given by (7) that certain coefficients Δ_j near the vicinity of the boundaries ($j = 0$ and $j = n - 1$) lie outside the time window $[0, t_f]$ defined by $j = 0, 1, \dots, n - 1$. These coefficients must be treated properly for finite domain analysis. Here, a wavelet based extrapolation scheme [Williams and Amaratunga 1997] is implemented for the solution of boundary value problems. This approach allows treatment of finite length data and uses polynomials to extrapolate the coefficients lying outside the finite domain either from interior coefficients or initial/boundary values. The method is particularly suitable for approximation in time, because of the ease of imposing initial values. The method converts the PDEs (7) to a set of coupled PDEs:

$$c_d^2 \left(\frac{\partial^2}{\partial r^2} + \frac{1}{r} \frac{\partial}{\partial r} + \frac{\partial^2}{\partial z^2} \right) \{\Delta_j\} = [\Gamma^1]^2 \{\Delta_j\}, \tag{9}$$

where Γ^1 is the first order connection coefficient matrix obtained after using the wavelet extrapolation technique. It should be mentioned here that though the connection coefficients matrix, Γ^2 , for the second order derivative can be obtained independently, here it is written as $[\Gamma^1]^2$ as it helps to impose the

initial conditions [Mitra and Gopalakrishnan 2005]. These coupled PDEs are decoupled using eigenvalue analysis, via

$$\Gamma^1 = \Phi \Pi \Phi^{-1},$$

where Π is the diagonal eigenvalue matrix and Φ is the eigenvectors matrix of Γ^1 . Let the eigenvalues be $i\gamma_j$, with $i = \sqrt{-1}$. The decoupled PDEs corresponding to Equations (9) are

$$c_d^2 \left(\frac{\partial^2}{\partial r^2} + \frac{1}{r} \frac{\partial}{\partial r} + \frac{\partial^2}{\partial z^2} \right) \widehat{\Delta}_j = -\gamma_j^2 \widehat{\Delta}_j \quad j = 0, 1, \dots, n-1, \tag{10}$$

where $\widehat{\Delta}_j$ is

$$\widehat{\Delta}_j = \Phi^{-1} \Delta_j.$$

Following the same steps, the final transformed form of (2) is

$$c_s^2 \left(\frac{\partial^2}{\partial r^2} + \frac{1}{r} \frac{\partial}{\partial r} - \frac{1}{r^2} + \frac{\partial^2}{\partial z^2} \right) \widehat{U}_{\theta j} = -\gamma_j^2 \widehat{U}_{\theta j} \quad j = 0, 1, \dots, n-1. \tag{11}$$

Similarly, the transformed form of the decoupled displacement equations (4) and force boundary conditions (5) can be written as

$$\nabla_1^2 \widehat{u}_j = \frac{\partial \widehat{\Delta}_j}{\partial r} + \frac{\partial \widehat{U}_{\theta j}}{\partial z}, \quad \nabla_0^2 \widehat{w}_j = \frac{\partial \widehat{\Delta}_j}{\partial z} - \frac{1}{r} \frac{\partial (r \widehat{U}_{\theta j})}{\partial r}, \tag{12}$$

$$\widehat{\sigma}_{rj} = \lambda \widehat{\Delta}_j + 2\mu \frac{\partial \widehat{u}_j}{\partial r}, \quad \widehat{\sigma}_{zj} = \mu \frac{\partial \widehat{u}_j}{\partial z} + \frac{\partial \widehat{w}_j}{\partial r}, \tag{13}$$

where $\widehat{\sigma}_{rj}$ and $\widehat{\sigma}_{zj}$ are the transformed forces $\sigma_r(r, z, t)$ and $\sigma_z(r, z, t)$ respectively.

2.4. Spatial approximation. As stated earlier, the next step involved is to further reduce each of the transformed and decoupled PDEs given by Equations (10) and (11) for $j = 0, 1, \dots, n-1$ to a set of coupled ODEs using the Daubechies scaling function approximation in the axial (z) direction. Similar to time approximation, the transformed variable $\widehat{\Delta}_j$ is discretized at m points in the spatial window $[0, L_z]$, where L_z is the length in z direction. Let $\zeta = 0, 1, \dots, m-1$ be the sampling points; then

$$z = \Delta z \zeta,$$

where Δz is the spatial interval between two sampling points. The function $\widehat{\Delta}_j(r, z)$ can be approximated by the scaling function $\varphi(\zeta)$ at an arbitrary scale as

$$\widehat{\Delta}_j(r, z) = \widehat{\Delta}_j(r, \zeta) = \sum_k \widehat{\Delta}_{lj}(r) \varphi(\zeta - l), \quad l \in \mathbb{Z},$$

where the $\widehat{\Delta}_{lj}(r, z)$ (written $\widehat{\Delta}_{lj}$ hereafter) are the approximation coefficients. Thus (10) can be written as

$$c_d^2 \left(\frac{d^2}{dr^2} + \frac{1}{r} \frac{d}{dr} \right) \widehat{\Delta}_{lj} \varphi(\zeta - l) + c_d^2 \frac{1}{\Delta z^2} \widehat{\Delta}_{lj} \varphi''(\zeta - l) = -\gamma_j^2 \widehat{\Delta}_{lj} \varphi(\zeta - l). \tag{14}$$

Taking the inner product on both sides of (14) with the translates of scaling functions $\varphi(\zeta - i)$, where $i = 0, 1, \dots, m - 1$ and using their orthogonal properties, we get m simultaneous ODEs:

$$c_d^2 \left(\frac{d^2}{dr^2} + \frac{1}{r} \frac{d}{dr} \right) \widehat{\Delta}_{ij} + c_d^2 \frac{1}{\Delta z^2} \sum_{l=i-N+2}^{i+N-2} \widehat{\Delta}_{ij} \Omega_{i-l}^2 = -\gamma_j^2 \widehat{\Delta}_{ij}, \quad i = 0, 1, \dots, m - 1, \quad (15)$$

where N is the order of the Daubechies wavelet and Ω_{i-l}^2 is the connection coefficient for second order derivative defined in Equations (8).

It can be seen from the ODEs given by (15), that, similar to time approximation, even here, certain coefficients $\widehat{\Delta}_{ij}$ near the vicinity of the boundaries ($i = 0$ and $i = m - 1$) lie outside the spatial window $[0, L_z]$ defined by $i = 0, 1, \dots, m - 1$. These coefficients must be treated properly for finite domain analysis. Here, however, unlike in the time approximation, these coefficients are obtained through periodic extension, but only for free lateral edges, while other boundary conditions can be imposed quite differently using a restrain matrix [Patton and Marks 1996; Chen et al. 1996]. The unrestrained (free-free) boundary conditions may also be imposed in a similar way using restrain matrix but it has been seen from the numerical experiments that the use of a periodic extension gives accurate results. In addition, it allows decoupling of the ODEs using eigenvalue analysis and thus reduces the computational cost. Here, after expressing the unknown coefficients lying outside the finite domain in terms of the inner coefficients considering periodic extension, the ODEs given by (15) can be written as a matrix equation of the form

$$c_d^2 \left(\frac{d^2}{dr^2} + \frac{1}{r} \frac{d}{dr} \right) \{\widehat{\Delta}_{ij}\} + c_d^2 [\Lambda^1]^2 \{\widehat{\Delta}_{ij}\} = -\gamma_j^2 \{\widehat{\Delta}_{ij}\}, \quad (16)$$

where $[\Lambda^1]$ is the first order connection coefficient matrix obtained after periodic extension, and it is of the form

$$[\Lambda^1] = \frac{1}{\Delta Y} \begin{bmatrix} \Omega_0^1 & \Omega_{-1}^1 & \dots & \Omega_{-N+2}^1 & \dots & \Omega_{N-2}^1 & \dots & \Omega_1^1 \\ \Omega_1^1 & \Omega_0^1 & \dots & \Omega_{-N+3}^1 & \dots & 0 & \dots & \Omega_2^1 \\ \vdots & \vdots & & \vdots & & \vdots & & \vdots \\ \Omega_{-1}^1 & \Omega_{-2}^1 & \dots & 0 & \dots & \Omega_{N-3}^1 & \dots & \Omega_0^1 \end{bmatrix}.$$

The coupled ODEs given by (16) are decoupled using eigenvalue analysis similar to that done in time approximation as

$$\Lambda^1 = \Psi \Upsilon \Psi^{-1},$$

where Υ is the diagonal eigenvalue matrix and Ψ is the eigenvectors matrix of Λ^1 . It should be mentioned here that matrix Λ^1 has a circulant form and its eigen parameters are known analytically [Davis 1963]. Let the eigenvalues be $i\beta_i$, then the decoupled ODEs corresponding to Equations (16) are

$$c_d^2 \left(\frac{d^2}{dr^2} + \frac{1}{r} \frac{d}{dr} - \beta_i^2 \right) \widetilde{\Delta}_{ij} = -\gamma_j^2 \widetilde{\Delta}_{ij}, \quad i = 0, 1, \dots, m - 1, \quad (17)$$

where $\widetilde{\Delta}_{ij} = \Psi^{-1} \widehat{\Delta}_{ij}$. Following similar steps, the final transformed form of (11) is given by

$$c_s^2 \left(\frac{d^2}{dr^2} + \frac{1}{r} \frac{d}{dr} - \frac{1}{r^2} - \beta_i^2 \right) \widetilde{\mathcal{U}}_{\theta ij} = -\gamma_j^2 \widetilde{\mathcal{U}}_{\theta ij}. \quad (18)$$

Similarly, the decoupled displacement equations (12) and boundary conditions (13) can be written as

$$\left(\frac{d^2}{dr^2} + \frac{1}{r} \frac{d}{dr} - \frac{1}{r^2} - \beta_i^2\right) \tilde{u}_{ij} = \frac{d\tilde{\Delta}_{ij}}{dr} - i\beta \tilde{\mathcal{U}}_{\theta ij}, \tag{19}$$

$$\left(\frac{d^2}{dr^2} + \frac{1}{r} \frac{d}{dr} - \beta_i^2\right) \tilde{w}_{ij} = -i\beta_i \tilde{\Delta}_{ij} - \frac{1}{r} \frac{d(r\tilde{\mathcal{U}}_{\theta ij})}{dr}, \tag{20}$$

$$\tilde{\sigma}_{rij} = \lambda \tilde{\Delta}_{ij} + 2\mu \frac{d\tilde{u}_{ij}}{dr}, \tag{21}$$

$$\tilde{\sigma}_{zij} = -i\beta_i \mu \tilde{u}_{ij} + \frac{d\tilde{w}_{ij}}{dr}. \tag{22}$$

The transformed and decoupled ODEs given by (17), (18) and (19)–(22) are used in the next two sections for frequency domain analysis and spectral finite element formulation.

3. Computation of wavenumbers

For wavenumber computation, the transformed differential equations (17) and (18) in terms of variables $\tilde{\Delta}_{ij}$ and $\tilde{\mathcal{U}}_{\theta ij}$ are to be expressed in terms of transformed displacements \tilde{u}_{ij} and \tilde{w}_{ij} using the relations given by Equations (3). Here, these transformed ODEs have coefficients that are functions of radius r unlike the governing equations for plate. That is, the wavenumber can be derived using a homogeneous assumption at a certain radius r . At a certain radius r , the solutions of the ODEs for \tilde{u}_{ij} and \tilde{w}_{ij} are of the form

$$\tilde{u}_{ij} = \sum_{k=1}^6 \bar{u}_{ij} e^{-ikr}, \quad \tilde{w}_{ij} = \sum_{k=1}^6 \bar{w}_{ij} e^{-ikr}, \tag{23}$$

where k is the wavenumber in the radial r direction and $\bar{u}_{ij}, \bar{w}_{ij}$ are functions of r . Hereafter, the subscripts i and j are dropped for simplified notation and all the following equations are valid for $j = 0, 1, \dots, n - 1$ and $i = 0, 1, \dots, m - 1$. By substituting (23) in the transformed ODEs obtained from Equations (17) and (18), the two polynomial equations in k become

$$\begin{aligned} (ic_d^2 k^3 - (2c_d^2 k^2/r) + i(\beta^2 c_d^2 - c_d^2/r - \gamma^2)k + (-3c_d^2/r^3 - c_d^2 \beta^2/r + \gamma^2/r))\bar{u} \\ + (-ic_d^2 \beta k^2 + (c_d^2 \beta/r)k + (ic_d^2 \beta^3 - i\beta \gamma^2))\bar{w} = 0, \\ (-ic_s^2 \beta k^2 + (-c_s^2 \beta/r)k - i(c_s^2/r^2 - c_s^2 \beta^2 + \gamma^2)\beta)\bar{u} + (-ic_s^2 k^3 + (c_s^2/r)k^2 - i(c_s^2/r + c_s^2 \beta^2 - \gamma^2)k)\bar{w} = 0. \end{aligned}$$

They can be solved to obtain the wavenumbers k for the spectrum relation, that is, the wavenumber-frequency relations at a certain radius r and axial wavenumber β . The solution can be performed easily by posing the problem as a Polynomial Eigenvalue Problem (PEP) similar to that done for FSFE formulation of a 2-D anisotropic plate in [Chakraborty and Gopalakrishnan 2005]. The PEP for this problem is of the form

$$\mathbf{A}_3 k^3 + \mathbf{A}_2 k^2 + \mathbf{A}_1 k + \mathbf{A}_0 = 0,$$

where $\mathbf{A}_3, \mathbf{A}_2, \mathbf{A}_1$ and \mathbf{A}_0 are 2×2 matrices. It should be restated here that the spectrum relations obtained from WSFE formulation are accurate up to a certain fraction of the Nyquist frequency f_{Nyq} . This fraction p_N depends on the order N of the Daubechies scaling function used [Mitra and Gopalakrishnan 2006a].

4. Spectral finite element formulation

The degrees of freedom associated with the element formulation are shown in Figure 1. The element has two degrees of freedom per node, which are \tilde{u} and \tilde{w} . The two sets of decoupled ODEs given by Equations (17) and (18) and the displacement relations Equations (19) and (20) are to be solved for \tilde{u} and \tilde{w} . The actual solutions $u(r, z, t)$ and $w(r, z, t)$ are obtained using inverse wavelet transform twice for temporal and spatial (axial) dimensions. For the finite length data, the wavelet transform and its inverse can be obtained using a transformation matrix given by [Williams and Amaratunga 1994].

Here, the Bessel's functions are used for the solution of the transformed governing equation given by Equations (17) and (18). The solutions for $\tilde{\Delta}$ and \tilde{U}_θ are obtained as

$$\tilde{\Delta}(r) = C_1 J_0(k_e r) + C_2 Y_0(k_e r), \quad \tilde{U}_\theta(r) = C_3 J_1(k_s r) + C_4 Y_1(k_s r), \quad (24)$$

where $k_e^2 = (\gamma^2/c_d^2 - \beta^2)$, $k_s^2 = (\gamma^2/c_s^2 - \beta^2)$ and C_1, C_2, C_3, C_4 are constants. J_n and Y_n are Bessel's functions of first and second kinds.

Substituting (24) in (19), (20) and solving for \tilde{u} and \tilde{w} gives (see [Heimann and Kolsky 1966])

$$\begin{aligned} \tilde{u}(r) &= -k_e (C_1 J_1(k_e r) + C_2 Y_1(k_e r)) - i\beta (C_3 J_1(k_s r) + C_4 Y_1(k_s r)), \\ \tilde{w}(r) &= -i\beta (C_1 J_0(k_e r) + C_2 Y_0(k_e r)) - k_s (C_3 J_0(k_s r) + C_4 Y_0(k_s r)). \end{aligned} \quad (25)$$

These solutions provide the interpolating functions for forming the elemental dynamic stiffness matrix. The unknown constants $\{\mathbf{a}\} = \{C_1, C_2, C_3, C_4\}$ can be determined from the transformed nodal displacements $\tilde{u}(r)$, $\tilde{w}(r)$ at inner ($r = r_i$) and outer ($r = r_o$) radii. The nodal displacement vector is $\{\tilde{\mathbf{u}}^e\} = \{\tilde{u}_1, \tilde{w}_1, \tilde{u}_2, \tilde{w}_2\}$, where $\tilde{u}_1 = \tilde{u}(r_i)$, $\tilde{w}_1 = \tilde{w}(r_i)$, $\tilde{u}_2 = \tilde{u}(r_o)$ and $\tilde{w}_2 = \tilde{w}(r_o)$. Thus we can relate nodal displacements and unknown constants from Equations (25) as

$$\{\tilde{\mathbf{u}}^e\} = [\mathbf{B}]\{\mathbf{a}\}. \quad (26)$$

Substituting (25) into the transformed force boundary conditions (21) and (22), we obtain

$$\begin{aligned} \tilde{\sigma}_r(r) &= (-\{(\lambda + 2\mu)k_e^2 - \lambda\beta^2\}J_0(k_e r) + 2\mu k_e^2 J_1(k_e r)/(k_e r))C_1 \\ &\quad + (-\{(\lambda + 2\mu)k_e^2 - \lambda\beta^2\}Y_0(k_e r) + 2\mu k_e^2 Y_1(k_e r)/(k_e r))C_2 \\ &\quad + 2i\mu k_s \beta (J_0(k_s r) - J_1(k_s r)/(k_s r))C_3 + 2i\mu k_s \beta (Y_0(k_s r) - Y_1(k_s r)/(k_s r))C_4 \end{aligned} \quad (27)$$

and

$$\tilde{\sigma}_z(r) = -2i\mu\beta k_e (J_1(k_e r)C_1 + Y_1(k_e r)) - \mu(k_s^2 - \beta^2)(J_1(k_s r)C_3 + Y_1(k_s r)C_4). \quad (28)$$

From these equations, we relate the nodal force vector $\{\mathbf{F}^e\} = \{\tilde{\sigma}_{r1}, \tilde{\sigma}_{z1}, \tilde{\sigma}_{r2}, \tilde{\sigma}_{z2}\}$ to the constants $\{\mathbf{a}\}$ as

$$\{\tilde{\mathbf{F}}^e\} = [\mathbf{C}]\{\mathbf{a}\}, \quad (29)$$

where $\tilde{\sigma}_{r1} = \tilde{\sigma}_r(r_i)$, $\tilde{\sigma}_{z1} = \tilde{\sigma}_z(r_i)$, $\tilde{\sigma}_{r2} = \tilde{\sigma}_r(r_o)$ and $\tilde{\sigma}_{z2} = \tilde{\sigma}_z(r_o)$. Finally, from (26) and (29), a relation between transformed nodal forces and displacements is obtained:

$$\{\tilde{\mathbf{F}}^e\} = [\mathbf{C}][\mathbf{B}]^{-1}\{\tilde{\mathbf{u}}^e\} = [\tilde{\mathbf{K}}^e]\{\tilde{\mathbf{u}}^e\},$$

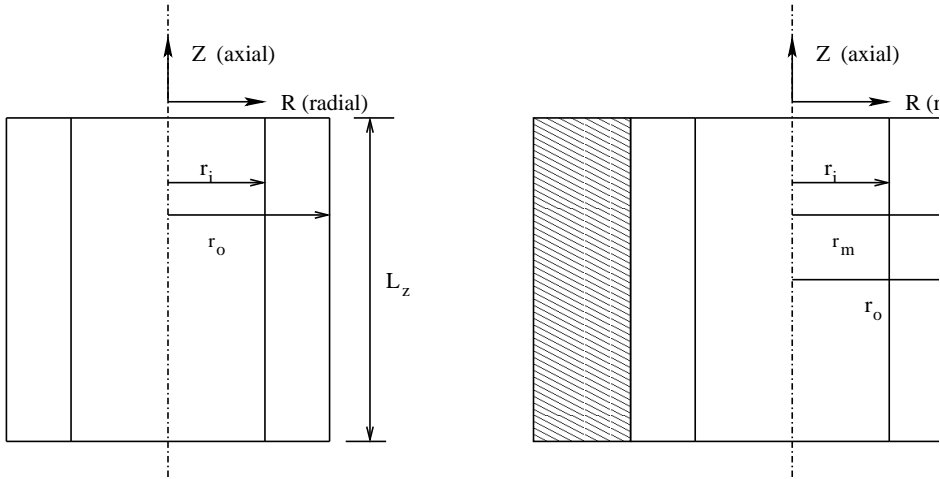


Figure 2. Aluminum (left) and aluminum-steel (right) hollow cylinders.

where $[\tilde{\mathbf{K}}^e]$ is the exact elemental dynamic stiffness matrix. These elemental dynamic stiffness matrices can be assembled in a similar way as in conventional FE to obtain the global stiffness matrix for the analysis of more complex structures.

5. Numerical experiments

In this section, the developed 2-D WSFE is used to analyze axisymmetric radial and axial wave propagations in isotropic cylinders due to broadband impulse excitation. First, the simulations are performed for an aluminum hollow cylinder free at both ends and internal and/or external pressure acting in radial/axial directions. The cylinder has an inner radius $r = r_i$, outer radius $r = r_o$ and the axial length is L_z , as shown in Figure 2, left. The loading conditions are shown in Figure 3. Examples are also presented

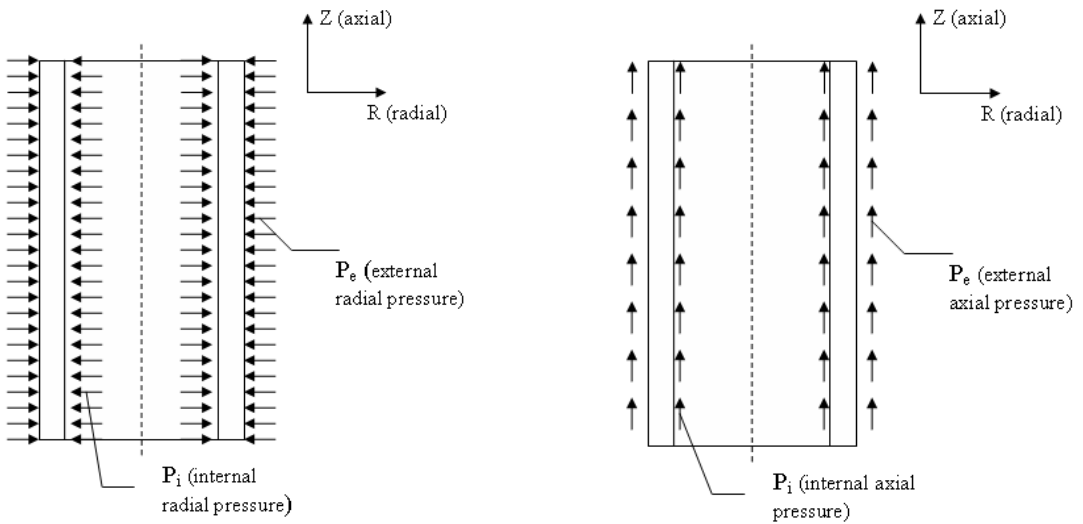


Figure 3. Radial (left) and axial (right) internal and external pressure.

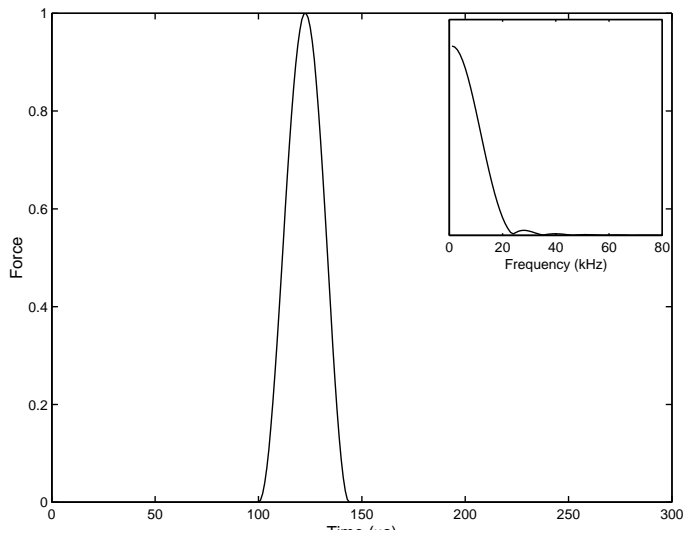


Figure 4. Impulse load in time and frequency (inset) domain.

where instead of uniform pressure, the radial/axial load acting along the axial direction has a pulse-like spatial (axial) distribution. Next, a more complex structure is considered for analysis, a cylinder made of a bimaterial, aluminum-steel (Figure 2, right). The material properties adopted for the aluminum and steel cylinders are: Young’s modulus, $E_a = 70$ GPa and $E_s = 200$ GPa; mass densities, $\rho_a = 2700$ kg/m³ and $\rho_s = 7860$ kg/m³; Poisson’s ratio, $\nu = 0.3$.

In all these results, the impulse load applied has unit amplitude and the time duration is $50 \mu s$, with a frequency content 44 kHz. The load is shown in the time and frequency domains in Figure 4.

The 2-D WSFE model is formulated with the Daubechies scaling function of order $N = 22$ for the temporal approximations and $N = 4$ for the spatial one. The time sampling rate $\Delta t = 2 \mu s$, unless otherwise mentioned, while the spatial sampling rate Δz is varied depending on L_z . As mentioned earlier, for the aluminum cylinder, only one 2-D WSFE is used to simulate the responses, independent of its dimensions. However, for the bimaterial cylinder in Figure 2, right, two elements are required for modeling, due to the discontinuity present in the problem.

5.1. Wavenumber computation. The spectrum relations for an aluminum hollow cylinder with $r_i = 0.02$ m and $r_o = 0.03$ m at different radii r obtained from the wavenumber computation discussed earlier are plotted in Figure 5. The three panels of the figure show the real or propagating part of the wavenumbers for $r = 0.02, 0.025$ and 0.03 m. These wavenumbers have significant imaginary parts which imply that the waves are inhomogeneous in nature, in other words, they attenuate while they propagate. As the radius is moved from inner to outer radius, the cut-off frequency which is the frequency at which the wavenumber is zero is also driven outward to a higher frequency. The wavenumbers are plotted for an axial wavenumber of $\beta = 50$ and are obtained with $\Delta t = 4 \mu s$ (Nyquist frequency of 125 kHz). However, as mentioned in [Mitra and Gopalakrishnan 2006a], WSFE predicts accurate wavenumbers only up to a certain fraction p_N of the Nyquist frequency f_{nyq} . This fraction depends only on the order of Daubechies scaling function N , and is approximately equal to 0.6 for $N = 22$. Thus, in Figure 5, the

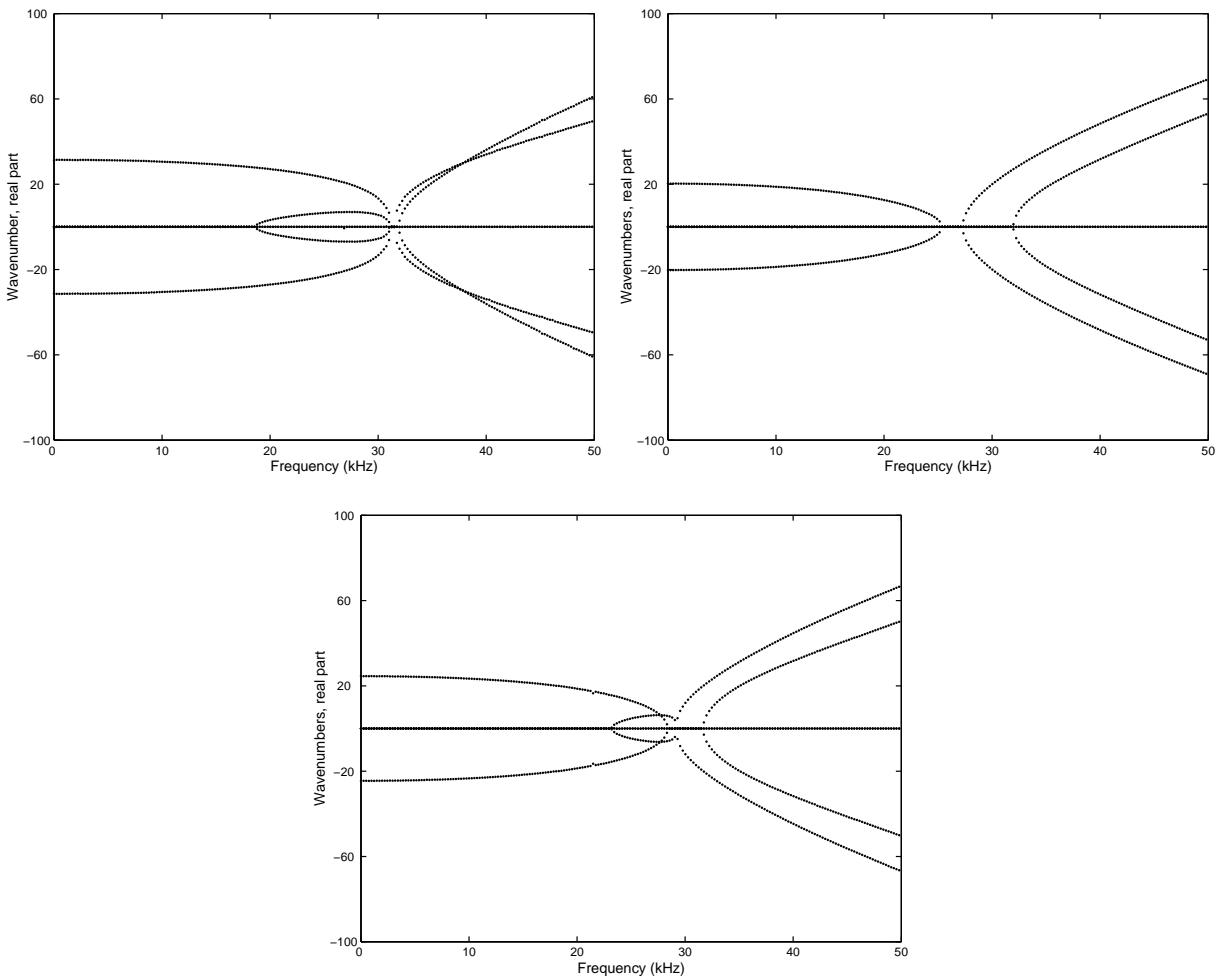


Figure 5. Real parts of wavenumbers at $r = r_i$ (top left), $r = \frac{1}{2}(r_i + r_o)$ (bottom) and $r = r_o$ (top right).

spectrum relations are plotted only up to 60 kHz, which is less than the allowable frequency range of $f_N = p_N f_{Nyq} = 75$ kHz.

5.2. Time domain analysis. Here, first the responses obtained using the formulated element are validated with 2-D FE analysis. Figure 6 compares the radial velocities for an aluminum cylinder with $r_i = 0.05$ m, $r_o = 0.1$ m and $L_z = 2.0$ m (see Figure 2, left) with 2-D FE results, showing the radial velocities at the midpoint (at $L_z/2$ from the free ends) and at inner $r = r_i$ and outer radii $r = r_o$ respectively. The applied load is the unit impulse, as shown in Figure 4. It is applied as a uniform pressure P_1 (Figure 3, left) in the radial direction along the inner surface ($r = r_i$). As an example, such internal pressure can be encountered in fluid carrying pipes and other cylindrical pressure vessels. The 2-D FE results are obtained using ANSYS 10.0, with a mesh consisting of 10220 four-noded quadrilateral axisymmetric elements (PLANE42). Newmarks' scheme with time step $2 \mu s$ is used for time integration. A further

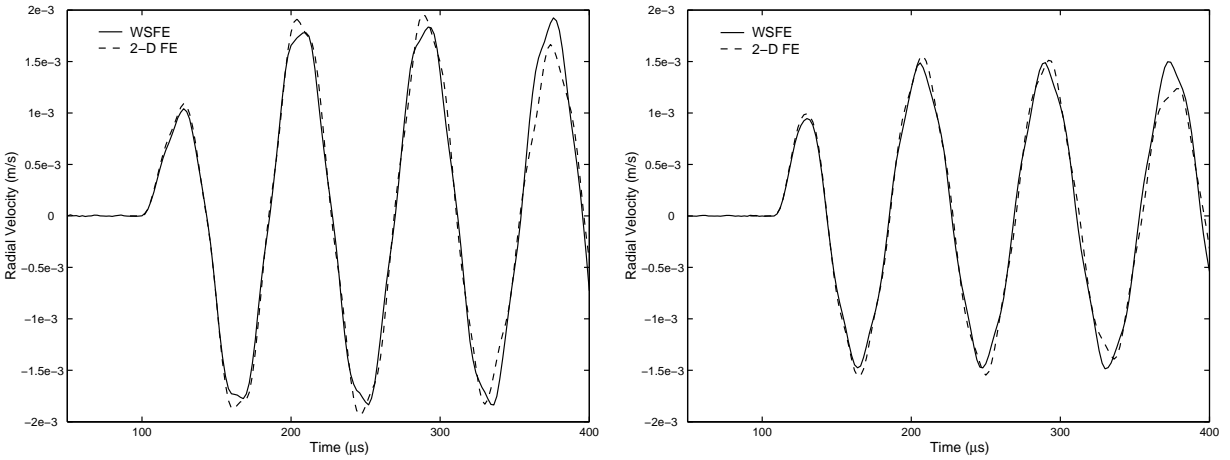


Figure 6. Radial velocities at midpoint along the axial direction at $r = r_i$ (left) and $r = r_o$ (right), due to internal radial pressure.

refinement of the FE mesh does not give significant difference in results. WSFE for this example is formulated with $N = 22$, time interval $\Delta t = 2 \mu s$ and time window $T_w = 512 \mu s$. Unlike FSFE, here the accuracy of the simulation is independent of the time window T_w because the present method is free from the wrap-around problem. Here T_w is chosen as required for observation. The number of discretization steps in the axial direction is $m = 128$ and thus the spatial sampling rate is $\Delta z = 0.0039$ m. Here only one WSFE is used for modeling as it was mentioned earlier, that is in absence of any discontinuities, only one WSFE is capable of modeling the entire structure irrespective of its dimensions. In the case of FSFE, the axial dimension is considered to be infinite or unbounded. It can be observed from these plots that the WSFE results match well with the corresponding 2-D FE results. Similar axial velocity responses

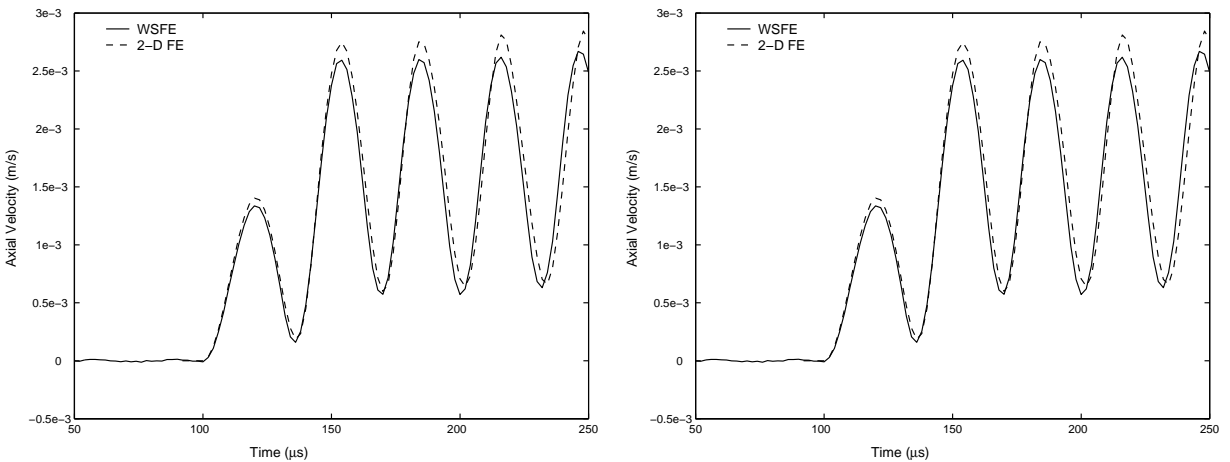


Figure 7. Axial velocities at midpoint along the axial direction at $r = r_i$ (left) and $r = r_o$ (right), due to internal axial pressure.

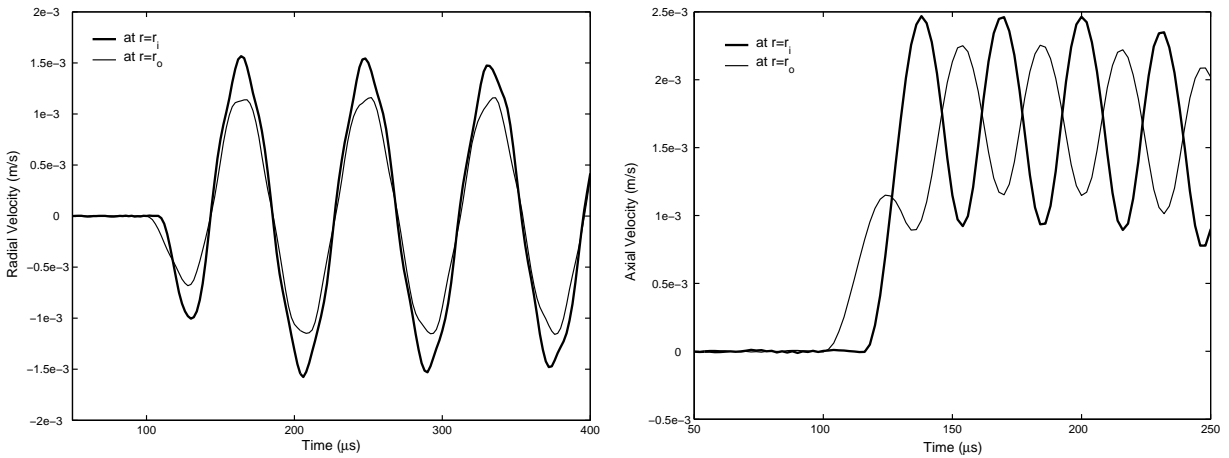


Figure 8. Radial (left) and axial (right) velocities at midpoint along the axial direction due to external radial and axial pressures respectively.

are plotted in Figure 7 under the same loading conditions as before, except that here they are applied in axial direction (Figure 3, right). The figure shows the axial velocities at $r = r_i$ and $r = r_o$ at distances $L_z/2$ from the free ends. Even here, the responses are validated with 2-D FE results and it can be seen that the responses compare very well. The modeling parameters for WSFE and the FE mesh are kept the same as in the previous case of radial velocities. Similar radial and axial velocities of the cylinder described above are plotted in Figure 8. However, here an external pressure P_e is considered instead of internal pressure as in previous example. This example is done to simulate the loading condition in a cylindrical excavation casing. The velocities are measured at midpoint at $L_z/2$ from the free end along the axial (z) direction at both inner $r = r_i$ and outer $r = r_o$ surfaces. Figure 9 plot similar radial and axial velocities, with the difference that the loading condition consists of both internal (P_i) and external (P_e) pressures.

Next, WSFE is used to model a relatively complex structure of bimaterial, aluminum-steel cylinder. The configuration is shown in Figure 2, right, where the inner cylinder is composed of aluminum and is surrounded by a concentric steel cylinder. The innermost radius is $r_i = 0.05$ m, the radius of the interface is $r_m = 0.09$ m and the outermost radius is $r_o = 0.1$ m. The length of the cylinder is $L_z = 2.0$ m and the impulse load (see (30)) is applied uniformly at the inner surface $r = r_i$ as an internal pressure in the radial/axial directions. As stated earlier, two WSFEs are required to model the structure because of the presence of discontinuity. WSFE modeling involves $m = 64$ spatial sampling points. Figure 10 plots the radial and axial velocities measured at the midpoint ($L_z/2$) and $r = r_i$. The responses are also compared with those of an aluminum cylinder of the same dimensions. The amplitude of the incident wave for the aluminum cylinder is much more than that of the aluminum-steel cylinder as expected as the latter has a much higher stiffness. Comparisons are also provided with 2-D FE results for the aluminum-steel cylinder. The FE mesh and the Newmark's time integration scheme is the same as in the previous example. It can be seen that the response matches well with the FE results for both radial and axial wave

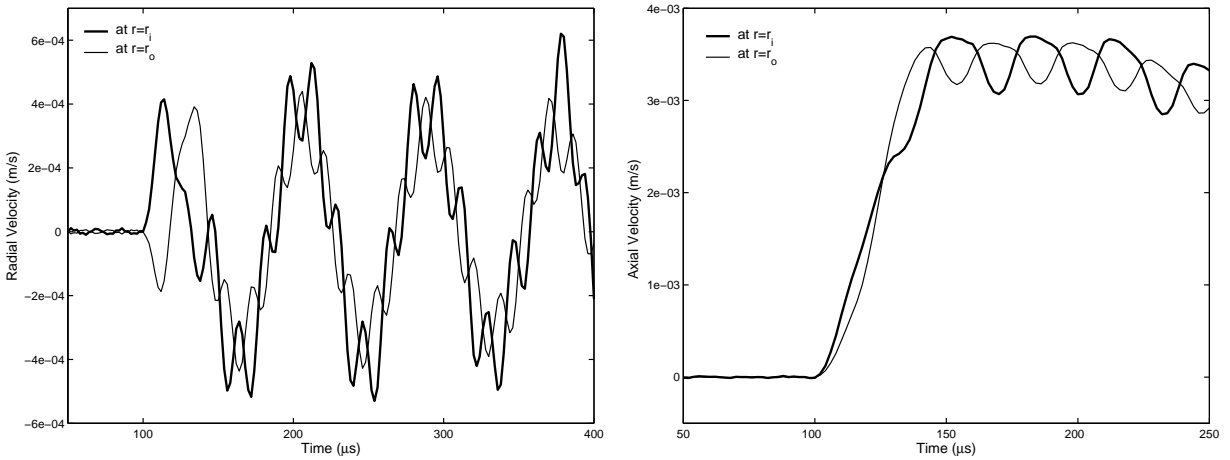


Figure 9. Radial (left) and axial (right) velocities at midpoint along the axial direction due to external and internal pressure in the radial and axial directions respectively.

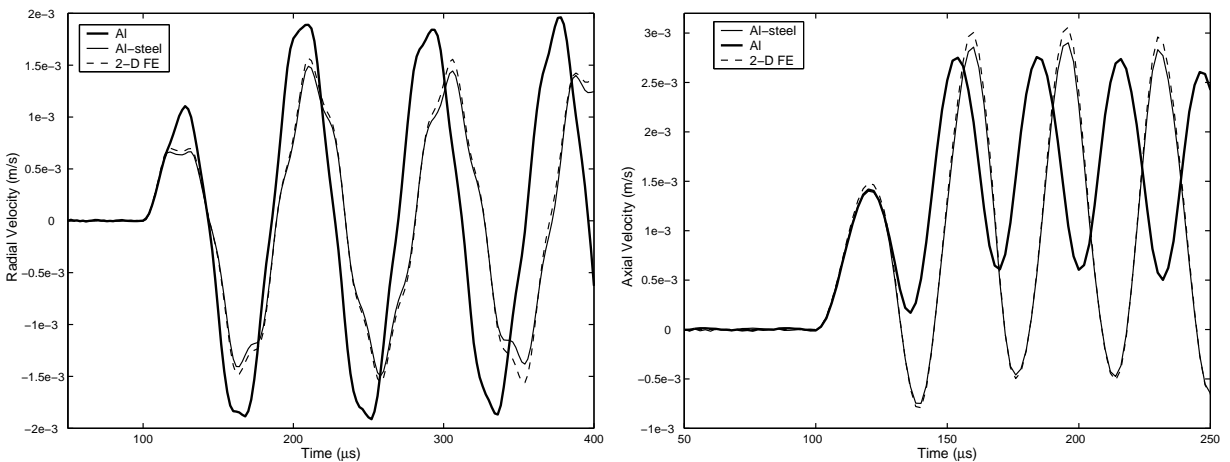


Figure 10. Radial (left) and axial (right) velocities in bimaterial Al-steel cylinder at midpoint along axial direction at $r = r_i$.

propagations. This numerical experiment is done with the purpose of emphasizing the efficiency of the proposed technique for modeling rather complex structures.

Next, instead of internal pressure, we apply an impulse load at the outer surface ($r = r_o$), with a pulse-like distribution along the axial direction, given by

$$F(z) = e^{-(z/\alpha)^2}, \tag{30}$$

where α is a constant and can be varied to change the pulse width in the z direction. Figure 11 compares the radial velocities in a hollow aluminum cylinder (with $r_i = 0.05$ m, $r_o = 0.1$ m and $L_z = 0.5$ m: see Figure 2, left) with 2-D FE results. The unit impulse load shown in Figure 4 is applied in the radial

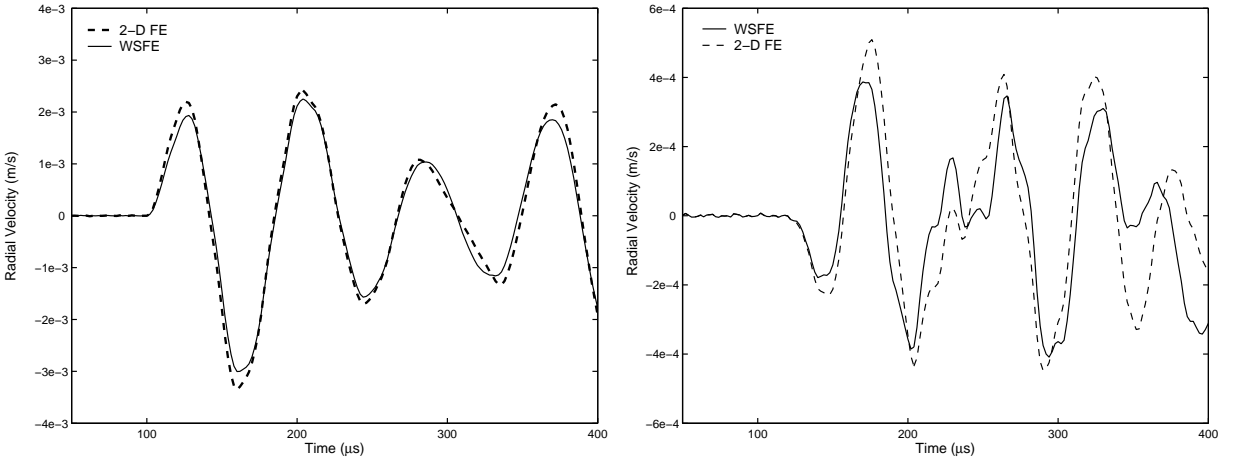


Figure 11. Radial velocities at midpoint (left) and quarter-point (right) along axial direction at $r = r_o$.

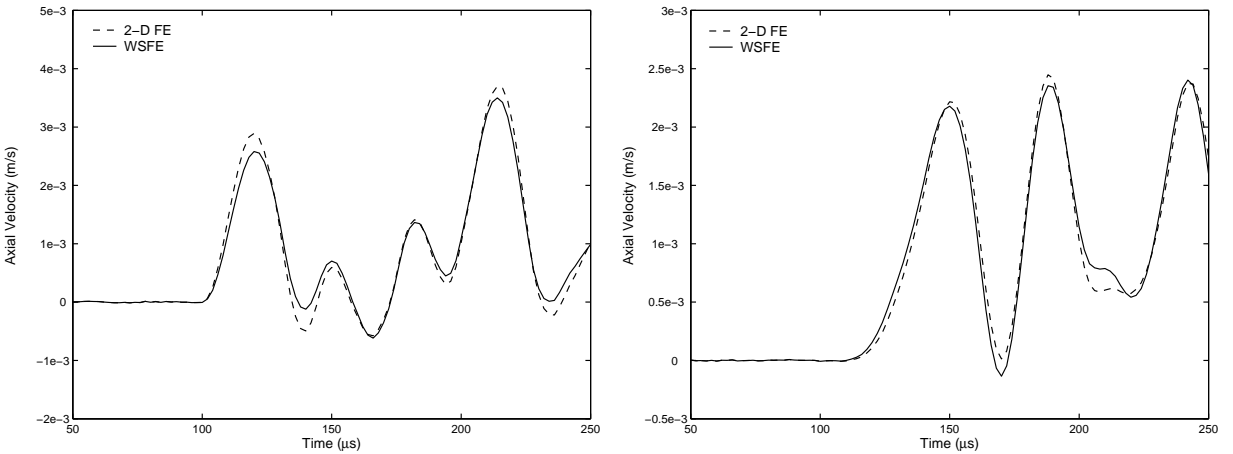


Figure 12. Axial velocities at midpoint (left) and quarter-point (right) along axial direction at $r = r_o$.

direction at $r = r_o$ and its distribution along the axial direction is given by (30) with $\alpha = 0.05$. The responses are simulated using a single WSFE with $m = 64$ sampling points in axial direction and thus spatial sampling rate is $\Delta z = 0.0078$ m. The 2-D FE analysis is done with ANSYS 10.0, with 2540, 4-noded quadrilateral axisymmetric elements (PLANE42) mesh. Time integration is performed with Newmarks scheme with time step $2 \mu s$. Figure 11 shows the radial velocities at $r = r_o$, half-way ($L_z/2$) and a quarter of the way ($L_z/4$) from the free ends. It can be seen that the responses obtained using the present method compares well with FE simulations. However, the difference between the results obtained from FE and WSFE simulations is more for the responses measured at the quarter-point and presented in Figure 11, right. A more refined mesh for FE analysis may give better correlation, but we

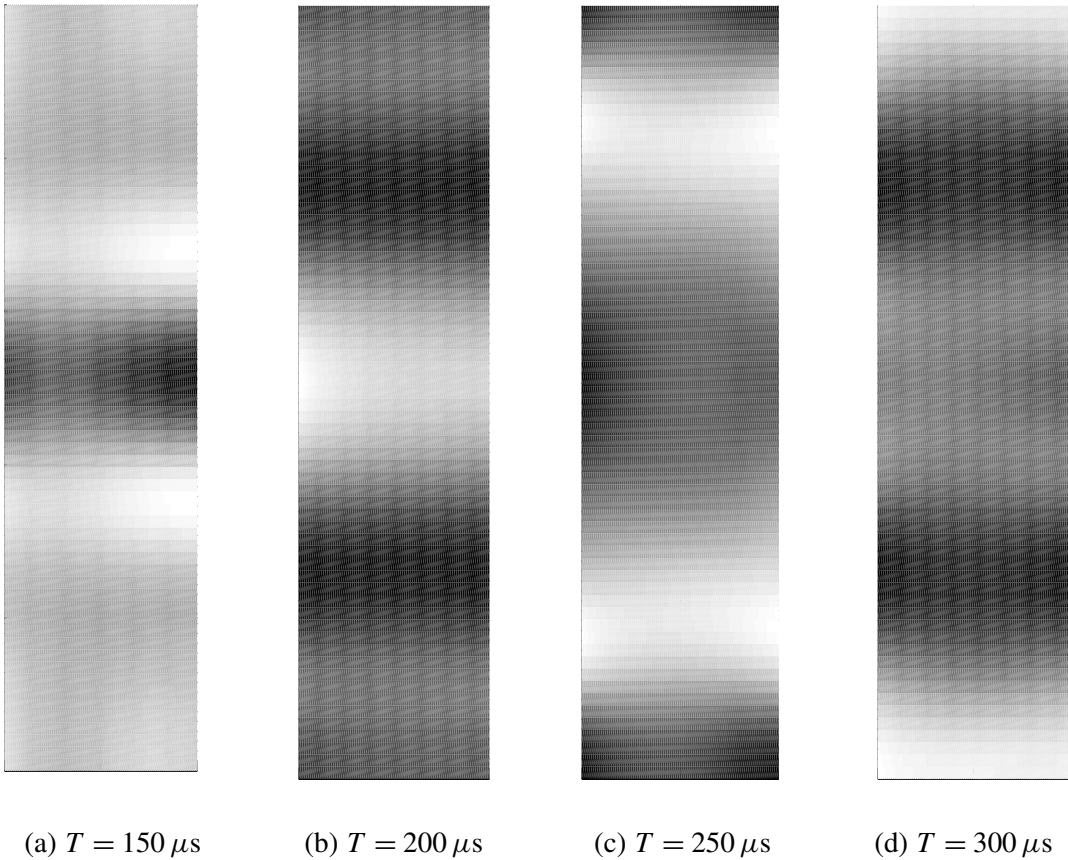


Figure 13. Snapshots of radial wave velocities. Vertical coordinate: axial direction, from 0 to 0.5 m; horizontal coordinate: radial direction, from 0.05 to 0.1 m.

have not used it in order to avoid the computational cost and because the comparisons are very good in all the other cases (Figure 11, left, and Figure 12). The latter figure plots the axial velocities when the load is applied in the axial direction. Even here, the results matches very well with those obtained from the FE analysis.

Figure 13 presents the snapshots of the radial velocities presented in Figure 11. Here, the thickness of the cylinder being more, the radial (and axial) variations of the radial wave velocities can be studied. The snapshots in Figure 13 are taken at $T = 150, 200, 250$ and $300 \mu s$, the impulse load having been applied at $100 \mu s$ with the peak unit amplitude at $125 \mu s$ (Figure 4). The figure shows the pattern of propagation of radial waves in both axial and radial directions due to the loading as described before for Figure 11. Such snapshots help to obtain the wave velocities at any spatial location at a given instance of time. For example, the snapshot at $T = 150 \mu s$ shows that at this time the incident radial wave has propagated along the axial direction and also the position of occurrence of maximum velocity can be obtained. At later times, say, $T = 300 \mu s$, the profile of wave propagation includes waves resulting from reflections at the boundaries. Similar interpretations can be given for the other snapshots. Note that the velocities

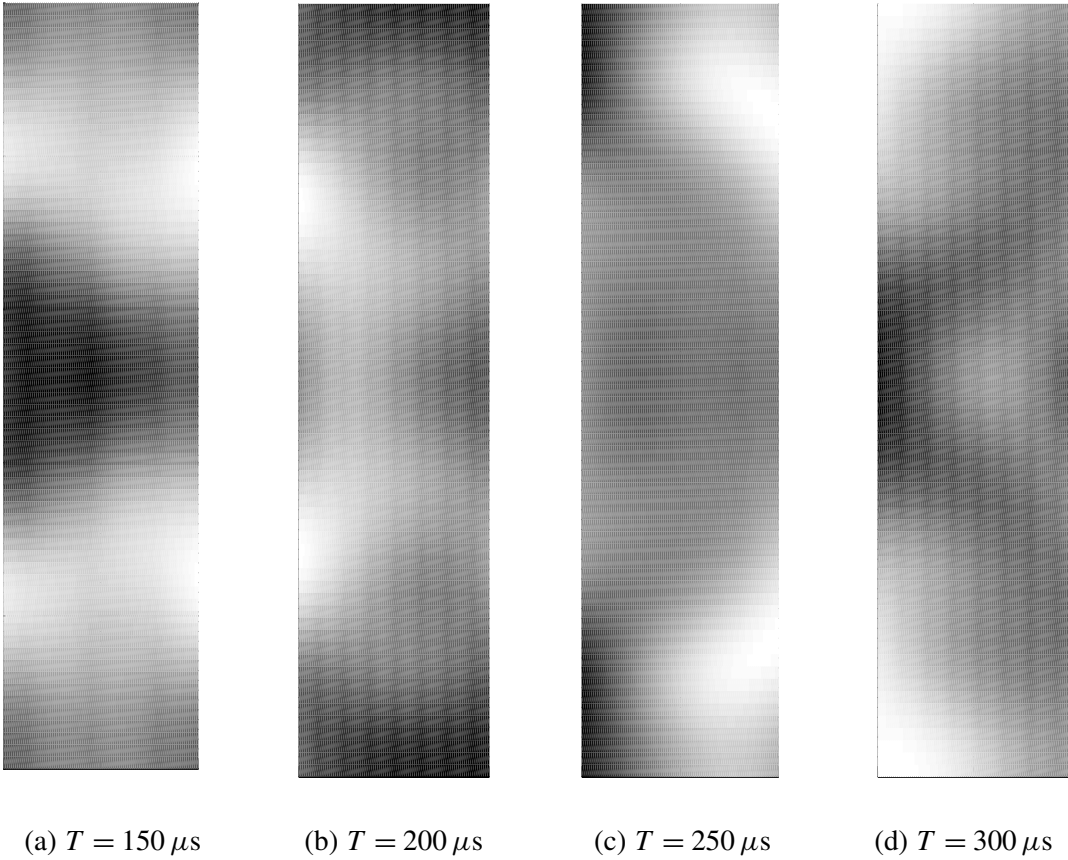


Figure 14. Snapshots of axial wave velocities. Vertical coordinate: axial direction, from 0 to 0.5 m; horizontal coordinate: radial direction, from 0.05 to 0.1 m.

at all the sampling points along the axial direction and at any points on the radial direction R required for the snapshots are obtained from a single simulation.

Snapshots for axial velocities due to loads applied in the axial direction are plotted in Figure 14. The loading conditions, structural properties and modeling parameters are as before. Again, snapshots at $T = 150, 200, 250$ and $300 \mu s$ are shown.

6. Conclusions

Here, a 2-D wavelet spectral element is developed for wave propagation analysis in isotropic axisymmetric cylinders. The conventional FE technique for such transient high frequency dynamics is not computationally viable and the spectral finite element method provides an efficient alternative. The use of localized Daubechies compactly supported wavelets as basis functions helps to overcome several important drawbacks of the prevalent FFT based spectral finite element method while retains the advantages of computational efficiency, simultaneous time and frequency domains analysis. Firstly, WSFE method can accurately model finite dimension structures unlike FSFE, which can only model 2-D structures

unbounded in one direction. Next, WSFE is free from wrap around problems associated with FSFE due to its periodicity assumption in temporal approximation. Consequently, FSFE, unlike WSFE cannot handle undamped finite length structures and even in presence of damping, larger time window is needed to remove distortions arising from wrap-around.

In this paper, radial and axial wave propagations in hollow isotropic cylinders of finite dimensions are studied in time and frequency domains. The time domain responses are validated with 2-D axisymmetric FE analysis and good comparison is observed. Next, the radial and axial distributions of the wave velocities are studied in cylinder of different configurations. Finally, the wave propagation analysis in a bimaterial cylinder is performed to show the ease of the proposed modeling technique in modeling more complicated structures.

References

- [Bao et al. 1999] X. L. Bao, P. K. Raju, and H. Uberall, "Circumferential waves on an immersed, fluid filled elastic cylindrical shell", *J. Acoust. Soc. Am.* **105**:5 (1999), 2704–2709.
- [Beylkin 1992] G. Beylkin, "On the representation of operators in bases of compactly supported wavelets", *SIAM J. Numer. Anal.* **29**:6 (1992), 1716–1740.
- [Chakraborty and Gopalakrishnan 2005] A. Chakraborty and S. Gopalakrishnan, "A spectrally formulated plate element for wave propagation analysis in anisotropic material", *Comput. Methods Appl. Mech. Eng.* **194**:42-44 (2005), 4425–4446.
- [Chen et al. 1996] M. Q. Chen, C. Hwang, and Y. P. Shih, "The computation of wavelet-Galerkin approximation on a bounded interval", *Int. J. Numer. Methods Eng.* **39**:17 (1996), 2921–2944.
- [Daubechies 1992] I. Daubechies, *Ten lectures on wavelets*, CBMS-NSF series in applied mathematics, SIAM, Philadelphia, 1992.
- [Davis 1963] P. J. Davis, *Interpolation and approximation*, Blaisdell, New York, 1963.
- [Doyle 1999] J. F. Doyle, *Wave propagation in structures*, Springer, New York, 1999.
- [El-Raheb 2005] M. El-Raheb, "Transient waves in an inhomogeneous hollow infinite cylinder", *Int. J. Solids Struct.* **42**:20 (2005), 5356–5376.
- [Godinho et al. 2003] L. M. C. Godinho, A. Tadeu, and F. Branco, "Wave scattering by infinite cylindrical shell structures submerged in a fluid medium", *Wave Motion* **38**:2 (2003), 131–149.
- [Godinho et al. 2004] L. M. C. Godinho, A. Tadeu, and F. Branco, "Dynamic analysis of submerged fluid-filled pipelines subjected to a point pressure load", *J. Sound Vib.* **271**:1–2 (2004), 257–277.
- [Heimann and Kolsky 1966] J. H. Heimann and H. Kolsky, "The propagation of elastic waves in thin cylindrical shells", *J. Mech. Phys. Solids* **14**:3 (1966), 121–130.
- [Mahan 2002] G. D. Mahan, "Oscillations of a thin hollow cylinder: carbon nanotubes", *Phys. Rev. B* **65**:23 (2002), 235402–235409.
- [Mitra and Gopalakrishnan 2005] M. Mitra and S. Gopalakrishnan, "Spectrally formulated wavelet finite element for wave propagation and impact force identification in connected 1-D waveguides", *Int. J. Solids Struct.* **42**:16-17 (2005), 4695–4721.
- [Mitra and Gopalakrishnan 2006a] M. Mitra and S. Gopalakrishnan, "Extraction of wave characteristics from wavelet based spectral finite element formulation", *Mech. Syst. Signal Process.* **20**:8 (2006), 2046–2079.
- [Mitra and Gopalakrishnan 2006b] M. Mitra and S. Gopalakrishnan, "Wavelet based 2-D spectral finite element for wave propagation analysis in isotropic plates", *CMES—Comp. Model. Eng. Sc.* **15**:1 (2006), 49–67.
- [Mitra and Gopalakrishnan 2006c] M. Mitra and S. Gopalakrishnan, "Wavelet based 2-D spectral finite element formulation for wave propagation analysis in isotropic plates", *Comput. Model. Eng. Sci.* **15**:1 (2006), 49–68.
- [Patton and Marks 1996] R. D. Patton and P. C. Marks, "One dimensional finite elements based on the Daubechies family of wavelets", *AIAA J.* **34**:8 (1996), 1696–1698.

- [Wang et al. 2005] C. Y. Wang, C. Q. Ru, and A. Mioduchowski, “Axisymmetric and beam-like vibrations of multi-wall carbon nanotubes”, *Phys. Rev. B* **72** (2005), 75414–75424.
- [Williams and Amaratunga 1994] J. R. Williams and K. Amaratunga, “Introduction to wavelets in engineering”, *Int. J. Numer. Methods Eng.* **37**:14 (1994), 2365–2388.
- [Williams and Amaratunga 1997] J. R. Williams and K. Amaratunga, “A discrete wavelet transform without edge effects using wavelet extrapolation”, *J. Fourier Anal. Appl.* **3**:4 (1997), 435–449.
- [Yin and Yue 2002] X. Yin and Z. Yue, “Transient plane-strain response of multilayered elastic cylinders to axisymmetric impulse”, *J. Appl. Mech. (Trans. ASME)* **69**:6 (2002), 825–835.

Received 27 Jun 2006. Accepted 15 Sep 2006.

MIRA MITRA: mira@aero.iisc.ernet.in

Department of Aerospace Engineering, Indian Institute of Science, Bangalore 560 012, India
<http://www.aero.iisc.ernet.in/~mira>

S. GOPALAKRISHNAN: krishnan@aero.iisc.ernet.in

Department of Aerospace Engineering, Indian Institute of Science, Bangalore 560 012, India